



The Flying Saucer: Tomography of the thermal and density gas structure of an edge-on protoplanetary disk

Anne Dutrey, S. Guilloteau, V. Piétu, E. Chapillon, Valentine Wakelam, E. Di Folco, T. Stoecklin, O. Denis-Alpizar, U. Gorti, R. Teague, et al.

► To cite this version:

Anne Dutrey, S. Guilloteau, V. Piétu, E. Chapillon, Valentine Wakelam, et al.. The Flying Saucer: Tomography of the thermal and density gas structure of an edge-on protoplanetary disk. *Astronomy and Astrophysics - A&A*, 2017, 607, pp.A130. 10.1051/0004-6361/201730645 . hal-01536626

HAL Id: hal-01536626

<https://hal.science/hal-01536626>

Submitted on 6 Oct 2020

HAL is a multi-disciplinary open access archive for the deposit and dissemination of scientific research documents, whether they are published or not. The documents may come from teaching and research institutions in France or abroad, or from public or private research centers.

L'archive ouverte pluridisciplinaire **HAL**, est destinée au dépôt et à la diffusion de documents scientifiques de niveau recherche, publiés ou non, émanant des établissements d'enseignement et de recherche français ou étrangers, des laboratoires publics ou privés.

The Flying Saucer: Tomography of the thermal and density gas structure of an edge-on protoplanetary disk

A. Dutrey¹, S. Guilloteau¹, V. Piétu², E. Chapillon^{1,2}, V. Wakelam¹, E. Di Folco¹, T. Stoecklin³, O. Denis-Alpizar⁴,
U. Gorti⁵, R. Teague⁶, T. Henning⁶, D. Semenov⁶, and N. Grosso⁷

¹ Laboratoire d'astrophysique de Bordeaux, Univ. Bordeaux, CNRS, B18N, Allée Geoffroy Saint-Hilaire, 33615 Pessac, France
e-mail: anne.dutrey@u-bordeaux.fr

² IRAM, 300 rue de la piscine, 38406 Saint Martin d'Hères, France

³ Institut des Sciences Moléculaires, UMR5255-CNRS, 351 Cours de la libération, 33405 Talence, France

⁴ Universidad Autónoma de Chile, Instituto de Ciencias Químicas Aplicadas, Theoretical and Quantum Chemistry Center,
2801 El Llano Subercaseaux, San Miguel, Santiago, Chile

⁵ SETI Institute/NASA Ames Research Center, Mail Stop 245-3, Moffett Field, CA 94035-1000, USA

⁶ Max-Planck-Institute für Astronomie, Königstuhl 17, 69117 Heidelberg, Germany

⁷ Observatoire Astronomique de Strasbourg, Université de Strasbourg, CNRS, UMR 7550, 11 rue de l'Université, 67000 Strasbourg, France

Received 17 February 2017 / Accepted 5 June 2017

ABSTRACT

Context. Determining the gas density and temperature structures of protoplanetary disks is a fundamental task in order to constrain planet formation theories. This is a challenging procedure and most determinations are based on model-dependent assumptions.

Aims. We attempt a direct determination of the radial and vertical temperature structure of the Flying Saucer disk, thanks to its favorable inclination of 90 degrees.

Methods. We present a method based on the tomographic study of an edge-on disk. Using ALMA, we observe at 0.5'' resolution the Flying Saucer in CO $J = 2-1$ and CS $J = 5-4$. This edge-on disk appears in silhouette against the CO $J = 2-1$ emission from background molecular clouds in ρ Oph. The combination of velocity gradients due to the Keplerian rotation of the disk and intensity variations in the CO background as a function of velocity provide a direct measure of the gas temperature as a function of radius and height above the disk mid-plane.

Results. The overall thermal structure is consistent with model predictions, with a cold (<12–15 K) CO-depleted mid-plane and a warmer disk atmosphere. However, we find evidence for CO gas along the mid-plane beyond a radius of about 200 au, coincident with a change of grain properties. Such behavior is expected in the case of efficient rise of UV penetration re-heating the disk and thus allowing CO thermal desorption or favoring direct CO photo-desorption. CO is also detected at up to 3–4 scale heights, while CS is confined to around 1 scale height above the mid-plane. The limits of the method due to finite spatial and spectral resolutions are also discussed.

Conclusions. This method appears to be a very promising way to determine the gas structure of planet-forming disks, provided that the molecular data have an angular resolution which is high enough, on the order of 0.3–0.1'' at the distance of the nearest star-forming regions.

Key words. circumstellar matter – protoplanetary disks – radio lines: stars

1. Introduction

Protoplanetary disks orbiting young pre-main sequence stars are the sites of planetary system formation. In these disks, gas represents about 99% of the mass and is mostly in the form of H₂. A minimum mass of 0.01 M_{\odot} was determined by Weidenschilling (1977) for the protosolar nebula based on the current solar system; since then models of planetary system formation have evolved drastically. Observational determinations of vertical and radial mass distribution of protoplanetary disks provide key constraints for planet formation models. Furthermore, studying the gas and dust distributions in protoplanetary disks found around low-mass T Tauri stars, recognized as young analogs to the solar system, has become a major challenge to understanding how planetary systems form and evolve.

With the advent of ALMA, many new results such as the observation of narrow dust rings in the HL Tau dust disk (ALMA Partnership et al. 2015) are changing our views on these objects. A series of studies of the disk associated with TW Hydrae – the closest T Tauri star – has significantly improved our understanding of disk physics and chemistry. This disk is seen almost face-on, maximizing its surface, and the dust and gas distributions have been intensively observed and modeled (Qi et al. 2004, 2013; Andrews et al. 2012, 2016; Rosenfeld et al. 2012; van Boekel et al. 2017; Teague et al. 2017). The $J = 1-0$ transition of HD, the hydrogen deuteride, has been also detected by Bergin et al. (2013) who determined the gas mass of the disk to be $>0.056 M_{\odot}$, a value ranging at the upper end of previous estimates based on indirect mass tracers (5×10^{-4} – $0.06 M_{\odot}$; Thi et al. 2010; Gorti et al. 2011). More recently

Teague et al. (2016) used simple molecules such as CO, CN, or CS to determine the turbulence inside the disk and found that the turbulent line broadening is less than 0.05 km s^{-1} . Schwarz et al. (2016) reanalyzed the HD observations and confirmed the high mass of the disk. However, both studies are limited by the knowledge of the disk's vertical structure, in particular the thermal profile of the gas, and assumptions have to be made on the vertical location of molecules since this cannot be directly recovered in a face-on disk.

Contrary to a face-on object, the disk around HD 163296, a Herbig Ae star of $2 M_{\odot}$, is inclined by about 45° along the line of sight. Such an inclination is enough to partially reveal the vertical location of the molecular layer, confirming that a significant fraction of the mid-plane is devoid of CO emission (de Gregorio-Monsalvo et al. 2013; Rosenfeld et al. 2013). In the case of IM Lupi, a $1 M_{\odot}$ star surrounded by a disk inclined by about 45° , a multi-line CO analysis coupled to a study of the dust disk (images and SED) allowed Cleeves et al. (2016) to provide a coherent picture of the gas and dust disk. However, owing to the combination of Keplerian shear and inclination, a complete determination of the vertical structure is challenging because at a given velocity there can be several locations (radii) inside the disk (see Beckwith & Sargent 1993). In other words, there is no perfect correspondence between a radius and a velocity and this generates degeneracies, which are particularly important when the spatial resolution is limited. A purely edge-on disk can allow the retrieval of the full vertical structure of the molecules from which the density and temperature vertical gradients can be derived, provided the angular resolution is high enough and the molecular transitions are adequately selected.

To test the ability of deriving the disk vertical structure from an edge-on disk, we submitted the ALMA project 2013.1.00387.S dedicated to the study of the Flying Saucer. The Flying Saucer (2MASS J16281370-2431391) is an isolated, edge-on disk in the outskirts of the ρ Oph dark cloud L 1688 (Grosso et al. 2003) with evidence for $5\text{--}10 \mu\text{m}$ -sized dust grains in the upper layers (Pontoppidan et al. 2007). Grosso et al. (2003) resolved the light scattered by micron-sized dust grains in the near-infrared with the ESO New Technology Telescope (NTT) and the Very Large Telescope (VLT) and estimated from the nebula extension dust a disk radius of $2.15''$, which is about 260 au for the adopted distance of 120 pc (Loinard et al. 2008). The detection of the CN $N = 2\text{--}1$ line (Reboussin et al. 2015) indicated the presence of a large gas disk. The ρ Oph region is crowded with molecular clouds that are strongly emitting in CO lines. The low extinction derived by Grosso et al. (2003) toward the Flying Saucer suggests that it lies in front of these clouds, and this is confirmed by the CO study of Guilloteau et al. (2016).

We observed CO $J = 2\text{--}1$, CS $J = 5\text{--}4$, and CN $N = 2\text{--}1$. This is a set of standard lines which has been extensively used to retrieve disk structures (Dartois et al. 2003; Piétu et al. 2007; Chapillon et al. 2012; Rosenfeld et al. 2013).

The dust and CO emissions detected in this ALMA project were partly discussed in Guilloteau et al. (2016) where we analyzed the absorption of the CO background cloud by the dust disk, deriving a dust temperature of about 7 K in the dust disk mid-plane at 100 au. This second paper deals with the retrieval of the gas temperature and density structures based on the analysis of the low angular resolution CO and CS lines. After showing the results and the analysis of the data, we then discuss the ability of using edge-on disks to determine the vertical structure of gas disks.

2. Observations

Imaging observations were performed with the Atacama Large mm/submm Array (ALMA) in a moderately compact configuration. The project 2013.1.00387.S was observed on 17 and 18 May 2015 under excellent weather conditions. The correlator was configured to deliver very high spectral resolution with a channel spacing of 15 kHz (and an effective velocity resolution of 40 m s^{-1}). We observed simultaneously CO $J = 2\text{--}1$, all the most intense hyperfine components of the CN $N = 2\text{--}1$ transition, and the CS $J = 5\text{--}4$ line.

Data was calibrated via the standard ALMA calibration script in the CASA software package (Version 4.2.2). Titan was used as a flux calibrator. The calibrated data was regridded in velocity to the Local Standard of Rest (LSR) frame using the “cvel” task, and exported through UVFITS format to the GILDAS package for imaging and data analysis. Atmospheric phase errors were small, providing high dynamic range continuum images and thermal noise limited spectral line data. The total continuum flux is 35 mJy at 242 GHz (with about 7% calibration uncertainty). With robust weighting, the uv coverage provided by the ~ 34 antennas yields a nearly circular beam size close to $0.5''$. The CS images were produced at an effective spectral resolution of 0.1 km s^{-1} ; the rms noise is 3 mJy/beam, i.e., about 0.27 K given the beam size of $0.48'' \times 0.46''$ at PA 53° . For CO, a spectral resolution of 0.08 km s^{-1} was used, and the rms noise is 4 mJy/beam, i.e., about 0.37 K given the beam size of $0.51'' \times 0.48''$ at PA 54° .

Figures 1 and 2 present the CO and CS channel maps, respectively, spectrally smoothed to 0.4 km s^{-1} for clarity. Figure 3 is a summary of the emission from CO, CS, and the dust continuum.

In addition, a CO $J = 2\text{--}1$ spectrum of the clouds along the line of sight was obtained with the IRAM 30 m telescope, as described in Guilloteau et al. (2016).

3. Results

The CO $J = 2\text{--}1$ and continuum results were partially reported by Guilloteau et al. (2016), who used them to measure the dust temperature.

3.1. Images

Figure 3 clearly shows that the disk is viewed close to edge-on. It also reveals a vertical stratification of the dust and molecules.

The modeling of the continuum image by Guilloteau et al. (2016) shows that the (millimeter) dust grains has a scale height of $12.7 \pm 0.3 \text{ au}$ at 100 au, increasing with a 0.34 ± 0.04 exponent. For comparison, the modeling of the near-infrared images by Grosso et al. (2003) shows that the (micron) dust grains have a larger scale height of $22.5 \pm 1.5 \text{ au}$ at 100 au when adopting the same definition and distance, and increasing more rapidly with a 1.25 exponent. Therefore, there is a clear indication of dust settling in this disk, with large grains preferentially close to the disk mid-plane.

The integrated intensity maps (Fig. 3) show that CS is significantly more confined towards the disk mid-plane than CO. As mentioned in Guilloteau et al. (2016), CO is contaminated by background emission from extended molecular clouds at four different velocities, which affects the derivation of the integrated emission and results in apparent asymmetries. The CS molecular emission extends up to radius of at least 300 au, and slightly more ($\sim 330 \text{ au}$) for CO. On the contrary, the dust emission is confined within 200 au. The apparent distributions may be more a result of temperature gradients, excitation conditions,

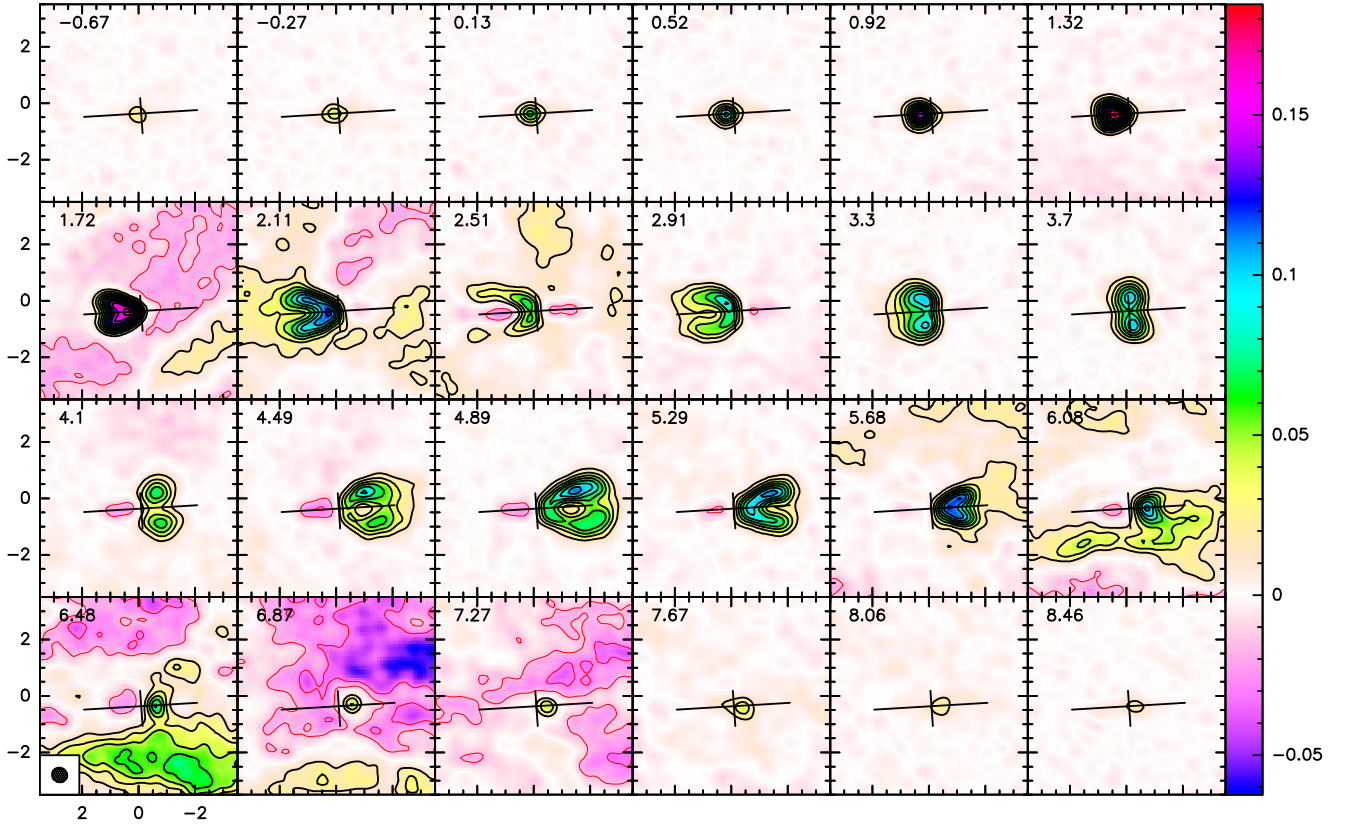


Fig. 1. Channel maps of the $^{12}\text{CO } J = 2-1$ line emission toward the Flying Saucer. Contours are in steps of 15 mJy/beam (1.22 K, approximately 7σ): negative contours are in red, positive contours in black, zero level contour omitted, and the color scale is given on the right. The cross indicates the position and orientation of the dust disk. The LSR velocity (in km s^{-1}) is indicated in the upper left corner of each panel.

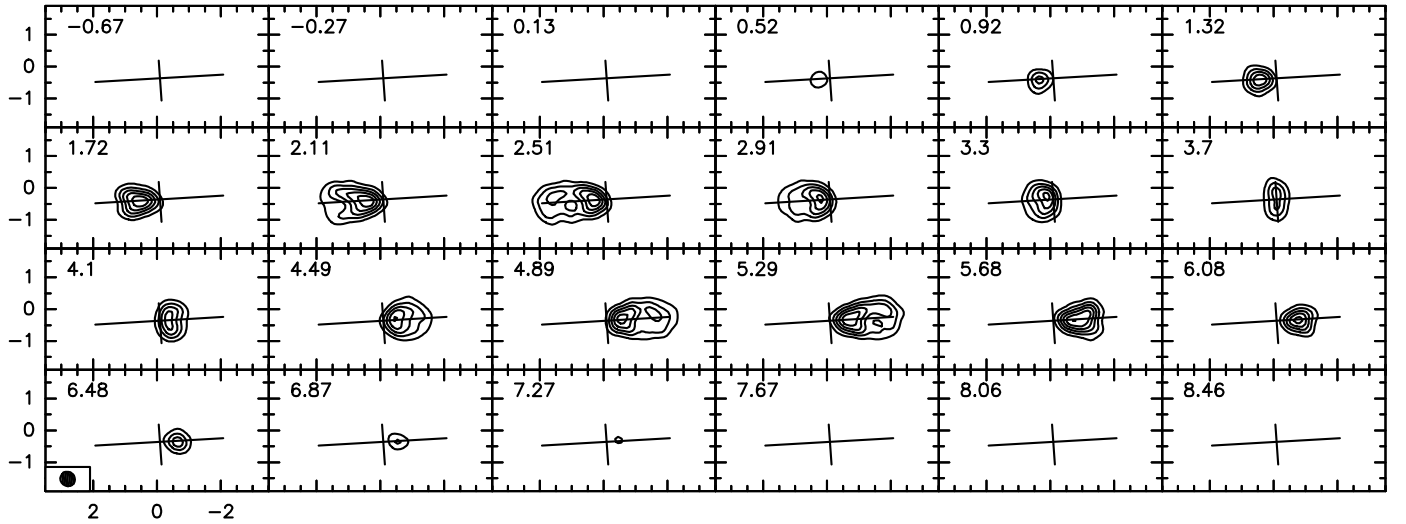


Fig. 2. As in Fig. 1, but for the $\text{CS } J = 5-4$ line. Contours are in steps of 15 mJy/beam (1.47 K, approximately 9σ).

and line opacities than of different abundance gradients for these molecules. The $\text{CO } J = 2-1$ line is much more optically thick than the CS line, and thus more sensitive to the (warmer) less dense gas high above the disk mid-plane. Along the mid-plane, self-absorption by colder, more distant gas, can result in lower apparent brightness. However, at the disk edges this effect should be small, so the higher brightness above the disk plane likely indicates a vertical temperature gradient with warmer gas above the plane.

The aspect of the iso-velocity contours (Fig. 3) is exactly what is expected from a Keplerian flared disk seen edge-on. In such a configuration, at an altitude z above the disk plane, the disk only extends inwards to an inner radius depending on z/H , where H is the scale height, so that the maximum velocity reached at altitude z is limited by this inner radius. Thus the mean velocity decreases from the mid-plane to higher altitude, resulting in a “butterfly” shape of the iso-velocity contours. The effect is less pronounced for CO, however, as its high optical depth

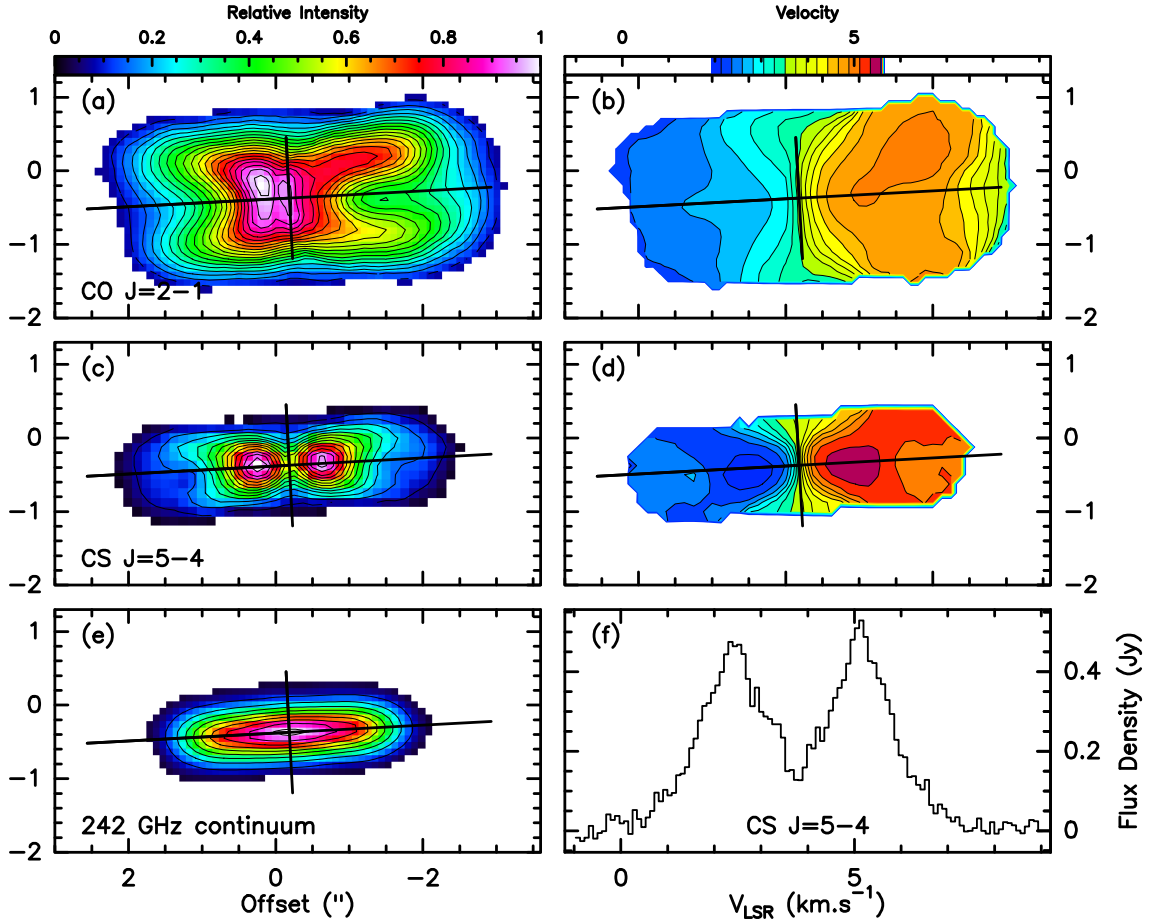


Fig. 3. Summary of the observations for CO, CS, and dust. CO $J = 2-1$ integrated intensity map (a) and isovelocity contours (b), CS $J = 5-4$ integrated intensity map (c) and isovelocity contours (d), continuum image at 242 GHz (e) and CS $J = 5-4$ integrated spectrum (f).

allows us to trace the emission well above the disk plane (isovelocity contours would be parallel for a cylindric distribution).

3.2. Simple determination of the disk parameters

To constrain the basic parameters of the disk, we made a simple model of the CS $J = 5-4$ emission with DiskFit (Piétu et al. 2007) assuming power laws for the CS surface density ($\Sigma_{\text{CS}}(r) = \Sigma_0(r/100 \text{ au})^{-p}$) and temperature $T_{\text{ex}}(r) = T_0(r/100 \text{ au})^{-q}$. The disk was assumed to have a sharp outer edge at R_{out} . The vertical density profile was assumed Gaussian (see Eq. (1) Piétu et al. 2007), with the scale height a (free) power law of radius $h(r) = H_0(r/100 \text{ au})^{-h}$. The line emission was computed assuming a (total) local line width dV independent of the radius and LTE (i.e., T_0 represent the rotation temperature of the level population distribution).

In addition to the above intrinsic parameters, the model also includes geometric parameters: the source position x_0, y_0 ; the inclination i and the position angle of the rotation axis PA; and the source systemic velocity V_{LSR} relative to the LSR frame.

Results are given in Table 1. This simple model allows us to determine the overall disk orientation, the systemic velocity, and the stellar mass, and gives an idea of the temperature required to provide sufficient emission. The apparent scale height H_0 derived at 100 au corresponds to a temperature of 53 K, much larger than T_0 . The difference may indicate that CS is substantially subthermally excited or, more likely, that CS emission only originates from above one hydrostatic scale height.

Table 1. CS disk modeling results.

Parameter	Value (at 100 au)	Unit	
PA	3.6 ± 0.4	$^\circ$	PA of disk rotation axis
i	85.4 ± 0.5	$^\circ$	Inclination
V_{LSR}	3.755 ± 0.003	km s^{-1}	Systemic velocity
M_*	0.58 ± 0.01	M_\odot	Star mass ^a
R_{out}	290 ± 7	au	Outer radius
dV	0.17 ± 0.01	km s^{-1}	Local line width ^b
Σ_0	$4.3 \times 10^{13} \pm 0.3 \times 10^{13}$	cm^{-2}	CS surface density
p	2.71 ± 0.03		Surface density exponent
T_0	18.0 ± 0.5	K	CS temperature
q	-0.18 ± 0.03		temperature exponent
H_0	25.8 ± 0.3	au	Scale height of CS ^c
h	-1.40 ± 0.03		Exponent of scale height

Notes. ^(a) Assuming Keplerian rotation. ^(b) Assumed constant with r . Errors are formal error bars from the fit. ^(c) Apparent scale height (see Sect. 3.2).

3.3. Position-velocity diagrams

A more detailed understanding of the disk properties can be derived from the position-velocity (PV) diagram shown in Figs. 4 and 5 where several altitudes z are shown. In these diagrams, radial straight lines (i.e., lines with $v(x) - V_{\text{disk}} \propto x$, where x is the impact parameter, v the velocity, and V_{disk} the disk systemic velocity) trace a constant radius r (see Appendix A for details). The blue straight lines indicate the outer radius ($R_{\text{out}} \approx 330 \text{ au}$). The blue curve is the Keplerian rotation curve $\sqrt{GM_*/r}$, with

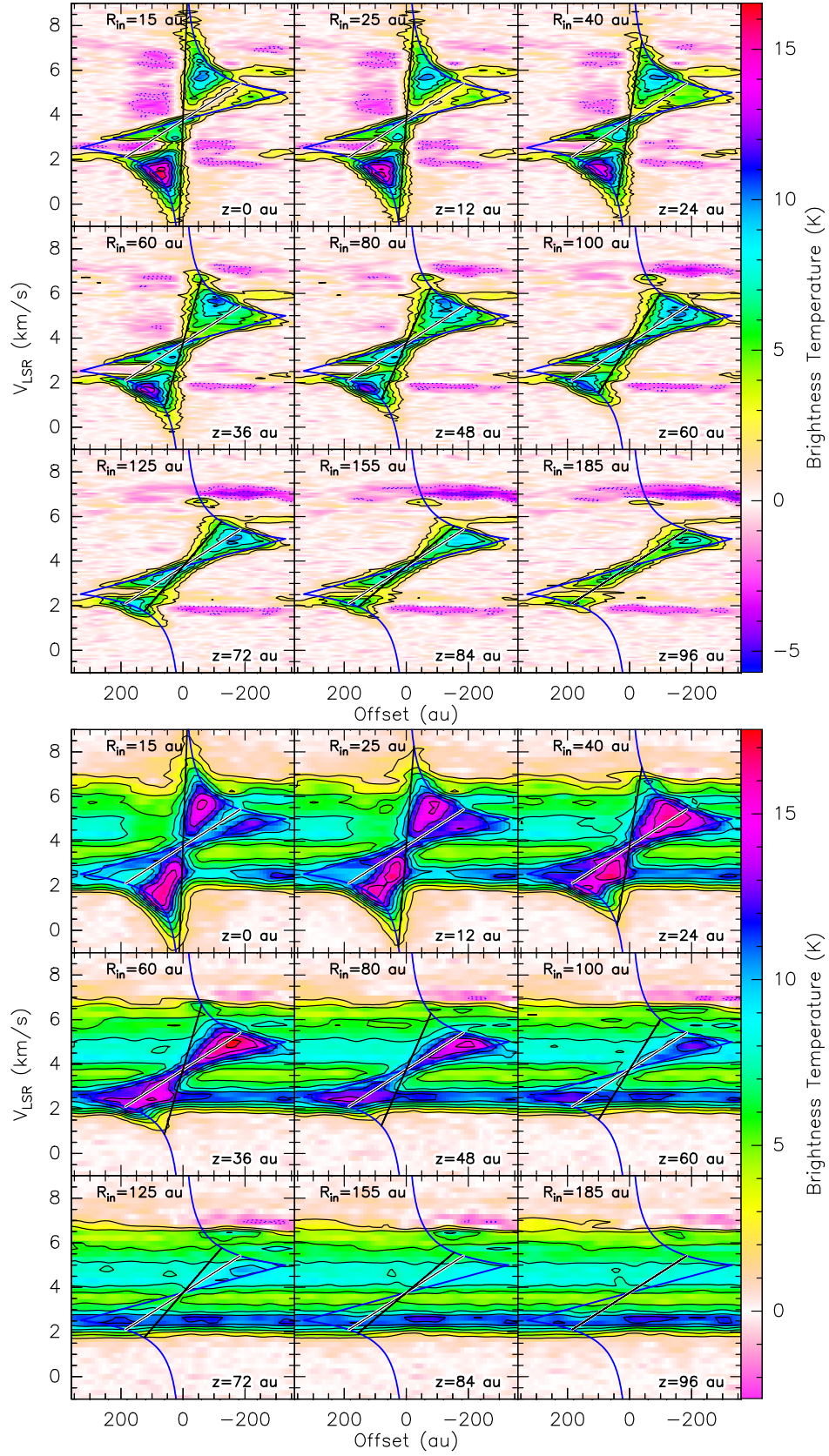


Fig. 4. Position-velocity diagram for CO $J = 2-1$. Each panel is a cut at a different height above the plane (indicated in the lower right corner of each panel). The spatial resolution is 56 au. *Top*: without the background added (spectral resolution 0.08 km s^{-1}). *Bottom*: with the background spectrum added. In each panel, the black line highlights the apparent inner radius whose value is quoted in the upper left corner. Here, the spectral resolution is 0.27 km s^{-1} .

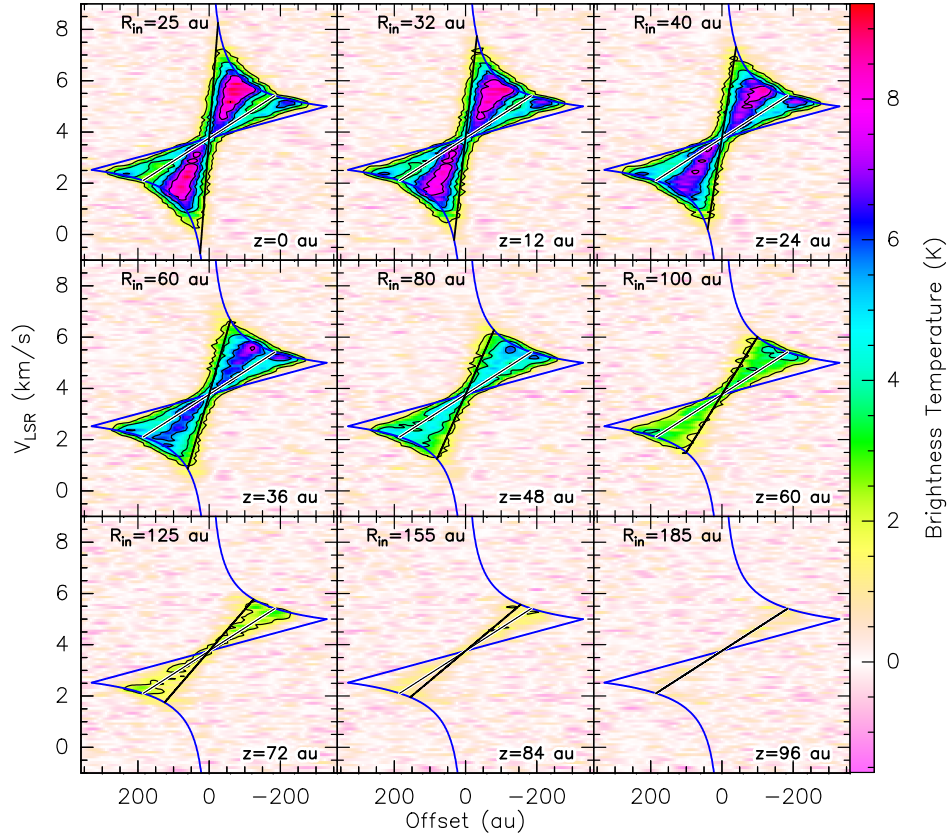


Fig. 5. As in Fig. 4, but for CS $J = 5-4$ (spectral resolution 0.10 km s^{-1}).

a stellar mass of $0.57 M_{\odot}$. The black line is the apparent inner radius R_{in} , and white-over-black line delineates the radius $r_{\text{dip}} \approx 185 \text{ au}$ where a dip in emission is observed at low altitudes both in CO and in CS.

The CO $J = 2-1$ line provides a direct view into the thermal structure of the disk. As is true for the continuum emission, the background provided by the four extended molecular clouds identified in the 30 m spectrum modulates the apparent brightness of the disk since the ALMA array only measures the difference in emission between the disk and the background clouds. Because the CO $J = 2-1$ line is essentially optically thick in disks, we can simply recover a corrected CO PV diagram by adding the background spectrum obtained with the IRAM 30 m (see [Guilloteau et al. 2016](#), their Fig. 1) to the observed CO emission, at least within the disk boundaries (in position and velocity). The result is given in Fig. 4 (bottom).

In the disk plane, while CO appears to extend down to very small radii ($< 15 \text{ au}$), CS may have an inner radius around 25 au.

At a given location, the impact of the finite beam size depends on the brightness temperature gradients, which are different for CO and CS (because of different opacities and excitation conditions), therefore leading to different apparent structures. Nevertheless, all apparent inner radii increase with height above the disk plane, as described before for the analysis of iso-velocity curves. This happens because the disk is flaring due to the hydrostatic equilibrium, hence its vertical thickness is increasing with radius.

The disk mid-plane is also clearly colder than the brightest background molecular cloud at 2.8 km s^{-1} , which has $J_v(T) = 11 \text{ K}$, beyond about 100 au radius, being almost as warm as the second brightest cloud at 4.2 km s^{-1} , with $J_v(T) = 8 \text{ K}$, at radii around 185 au. From this simple consideration, we safely

constrain the mean disk mid-plane temperature, averaged over one beam, to be 13 K near 180 au after proper conversion of the brightness temperature outside of the Rayleigh-Jeans domain. It would rise to about 18 K at 100 au.

The PV diagrams above the disk plane indicate a warmer temperature in the upper layers, since no absorption is visible for $z > 40 \text{ au}$ or so. Because of our limited linear resolution (about 56 au), with such a vertical temperature gradient the CO PV diagram only gives an upper limit to the disk mid-plane temperature because the scale height (about 10 au at 100 au) is substantially smaller than the linear resolution except at the disk edge.

We also note that CS and CO both show a drop in the emission intensity at radius $r_{\text{dip}} \approx 185 \text{ au}$. This drop is somewhat more difficult to identify in the CO PV diagrams because of the background clouds. In CO, the emission drop seems to disappear at a height of 40 au, suggesting it occurs only below about 30–40 au given the limited angular resolution. Beyond a radius of 220 au, CO emission is observed again. In CS, the deficit of emission near 185 au extends somewhat higher, up to a height of 60 au.

Figure 6 also reveals a north-south asymmetry, the north side being brighter in CS and in CO.

4. New method of analysis

4.1. Deriving the brightness distribution from the position-velocity diagram

For a homogeneous medium, the measured brightness temperature T_b is given by

$$T_b = (1 - \exp(-\tau))(J_v(T) - J_v(T_{\text{bg}})), \quad (1)$$

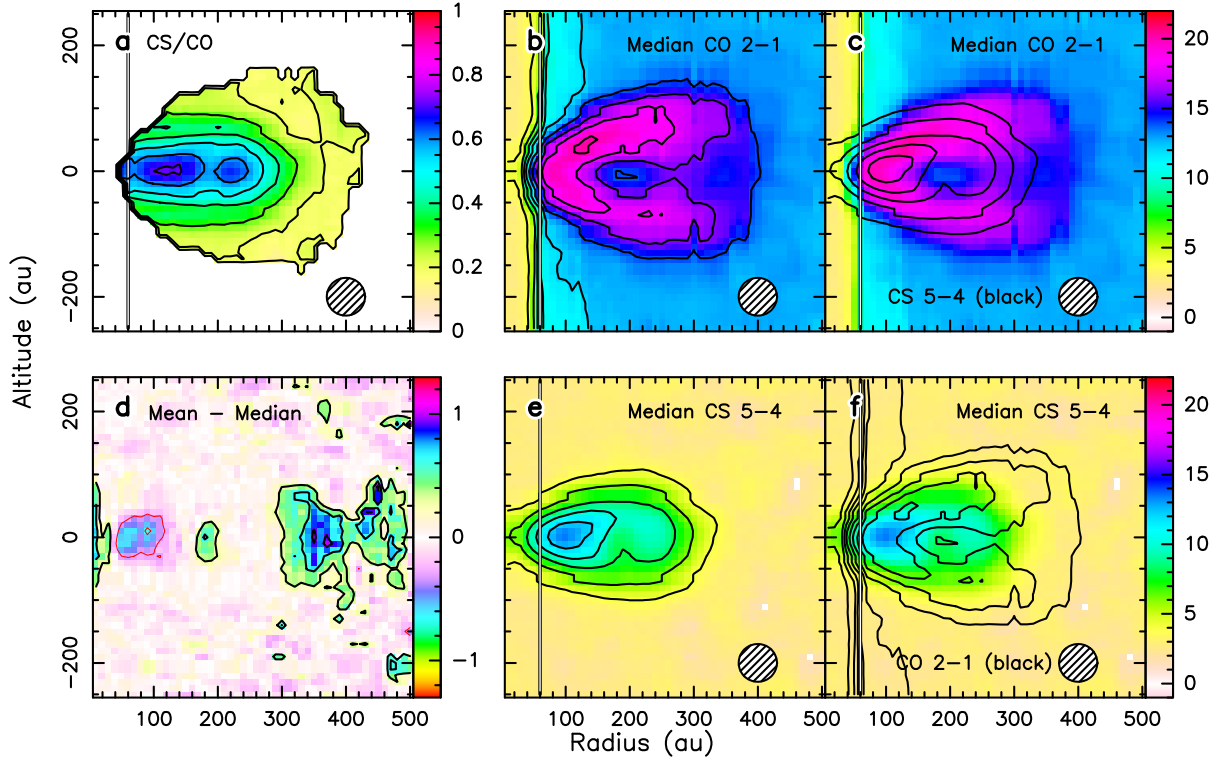


Fig. 6. Derivations of the gas temperature from the PV diagram. *a)* Ratio of the median TRD derived from CS over the median TRD derived from CO (contours are 0.1 to 1 by 0.1); *b)* CO median TRD, with contours from 4 to 22 K by spacing of 2 K; *c)* CO median TRD with contours of the CS median TRD overlaid; *d)* difference between the CS mean temperature and the CS median TRD (contours are -0.6 , -0.3 , 0.3 and 0.6 K); *e)* median CS TRD with contours from 4 to 12 K by spacing of 2 K; *f)* CS median TRD with contours of the CO median TRD. The spatial resolution is indicated. The vertical line delineates the area suffering from beam dilution.

where J_ν is the Planck function multiplied by $c^2/2k\nu^2$,

$$J_\nu(T) = \frac{h\nu}{k} \frac{1}{\exp(h\nu/(kT)) - 1}. \quad (2)$$

Since in a PV diagram a radial line represents a constant radius, we can recover the disk temperature from the thermalized and optically thick CO $J = 2-1$ transition by averaging the observed brightness along such radial lines in regions where the signal is sufficiently resolved spectrally and spatially. This averaging process yields the mean radiation temperature, $J_\nu(T) - J_\nu(T_{\text{bg}})$, from which the temperature T is derived. The disk being seen edge-on, cuts at various altitudes z provide a direct visualization of the gas temperature versus radius $T(r, z)$, although only at the angular resolution of the observations. The 2D image resulting from the application of this averaging process is called hereafter the tomographically reconstructed distribution (TRD).

While the CO $J = 2-1$ TRD is just the temperature distribution, for optically thinner or non-thermalized lines the interpretation is more complex because the TRD is a function of both the temperature and local density. Nevertheless, it also provides a direct measurement of the altitude of the molecular layer.

We use the PV diagrams of CO and CS transitions to derive their respective TRDs and show them in Fig. 6. The derivations were performed on data cubes without continuum subtraction because the subtraction, which was needed to compute the iso-velocity contours, may lead to substantial problems near the peak of the continuum. For CO, which is optically thick, the TRD(r, z) map is obtained using the PV diagram with the CO emission from the background clouds added since that emission is fully resolved out by the ALMA observations. This explains why the derived CO temperature brightness is on the order of

15 K around the disk, in agreement with the values derived from the CO spectrum taken with the IRAM 30 m radio telescope (Guilloteau et al. 2016).

In each case, we calculated a map of the mean, median, and maximum brightness along each radius. For CO, the mean and maximum brightness are contaminated by the background clouds, and the median is expected to be a better estimator. Furthermore, for CS, we found that the mean and the median always give results that differ by less than 1 K inside the disk at $r < 350$ au (see Fig. 6, panel (d), which shows the difference between the mean and the median for CS 5-4). This indicates that the derivations are robust and do not suffer from significant biases. The observed TRDs clearly confirm the location of the molecular layer above the mid-plane, but the CS emission peaks at a lower temperature and is located below the CO emission. The ratio of the CS TRD over the CO TRD confirms these behaviors (see Fig. 6, panel (a)).

The Keplerian shear implies that the spatial averaging of the derived brightness is not the same everywhere inside the disk. Indeed, at a radius r corresponding to a velocity $v(r)$, the smearing due to the Keplerian shear is given by $dr = 2r dv/v(r)$, where dv is the local linewidth, which is due to a combination of thermal and turbulent broadening. This limits the radial resolution which can be obtained in the disk outer parts. For instance, for CO, at 20 au, assuming a temperature of 30 K and a turbulent broadening (0.05 km s^{-1}) similar to that observed in the TW Hydrae disk by Teague et al. (2016), the dr would be on the order of ~ 2 au, a value that would not affect studies at spatial resolution down to $0.1''$ (12 au) or so. On the contrary, at radius 200 au, the dr would be on the order of 35 au for the same line width, dropping to 20 au assuming the same turbulence but a (mid-plane)

temperature of 7 K. This limits the gain obtained with high angular resolution only at large radii. It also explains why the apparent extent of the tomographically reconstructed distribution in Fig. 6 exceeds the disk outer radius more than expected from the angular resolution only.

Nevertheless, this smearing is purely radial and the vertical structure is not affected; the smearing is the same above and below the mid-plane at a given radius (assuming there is no vertical temperature gradient). This occurs because the disk is edge-on, but it is no longer true in less inclined disks. In such disks, the smearing resulting from the local line width will limit the effective resolution radially and vertically.

Finally, we note that this direct method of analysis, specific to edge-on disks, complements the classical channel maps studies by providing a more synthetic but direct view of the vertical disk structure.

4.2. CO modeling using DiskFit

To go beyond the resolution-limited information provided in Fig. 6, we study here the impact of several key parameters of the disk by performing grids of models to better constrain the disk geometry and structure. We use the ray-tracing model DiskFit (see Sect. 3.2, Piétu et al. 2007). For simplicity, we assume LTE conditions, which is appropriate for CO. Here the temperature structure is more complex than the simple vertically isothermal model described in Sect. 3.2. The atmosphere temperature is given by

$$T_{\text{atm}}(r) = T_{\text{atm}}^0 \left(\frac{r}{r_0} \right)^{-q_{\text{atm}}} \quad (3)$$

and the mid-plane temperature is given by

$$T_{\text{mid}}(r) = \min \left(T_{\text{atm}}(r), T_{\text{mid}}^0 \left(\frac{r}{r_0} \right)^{-q_{\text{mid}}} \right) \quad (4)$$

In between for an altitude of $z < z_q$, the temperature is defined by

$$T(r) = (T_{\text{atm}}(r) - T_{\text{mid}}(r)) \left(\cos \left(\frac{\pi z}{2z_q H(r)} \right) \right)^{2\delta} + T_{\text{mid}}(r), \quad (5)$$

where $H(r)$ is the hydrostatic scale height (defined by $T_{\text{mid}}(r)$). Provided $q_{\text{atm}} > q_{\text{mid}}$, there is a radius R_q beyond which the temperature becomes vertically isothermal. We note that for $q_{\text{mid}} = 0$, this definition is identical to that used by Dartois et al. (2003).

The models of the molecular emission were performed together with the continuum emission not subtracted. The continuum model uses, in particular for the density and temperature, the parameters defined in Table 1 of Guilloteau et al. (2016). We take into account the spatial resolution by convolving all models by a $0.5''$ circular beam. In all models, the outer radius r_{out} is taken at 330 au, in agreement with the value derived from the PV diagram.

We find that a small departure from edge-on inclination by 2–3 degrees is sufficient to explain the small north-south brightness asymmetry visible in Fig. 6. The most probable value is $i = 87^\circ$ (see Sect. 5.1), a value used for all further models.

In a first series of models, we assume a CO vertical distribution that follows the H_2 density distribution, i.e., assuming a constant abundance. For the H_2 density distribution, we assume either power laws or exponentially tapered distribution following the prescription given in Guilloteau et al. (2011). We explored

CO surface densities ranging from 10^{16} to 10^{19} cm^{-2} at 100 au. To account for the observed brightness at high altitudes above the disk plane, we find that the CO surface density at 100 au must be at least on the order of $5 \times 10^{17} \text{ cm}^{-2}$, with a power law index on the order of $p = 1.2$ for the radial distribution. We also explored the impact of the temperature distribution z_q , δ , T_{atm}^0 , q_{atm} , T_{mid}^0 , q_{mid} , and R_q . Best runs are obtained for mid-plane temperatures $T_{\text{mid}} \approx 10 \text{ K}$ at 100 au, $q_{\text{mid}} = 0.4$ leading to about 6 K at the outer disk radius, and 17 K at 26 au (CO snowline location), $T_{\text{atm}}^0 = 50 \text{ K}$, $q_{\text{atm}} = 0-0.2$, $\delta = 2$, and $z_q = 1.3-2$.

However, none of these models, which assume CO molecules are present everywhere in the disk, properly reproduces the CO depression observed around the mid-plane (see panel (b) of Fig. 6). This remains true even if the mid-plane temperature is set to values of 5–7 K, matching the temperature of large grains measured by Guilloteau et al. (2016).

We attempted to perform more realistic models by assuming complete molecular depletion (abundance $X_p(\text{CO}) = 0$) in the disk mid-plane. In this model, the zone where CO is present is delimited upwards by a depletion column density Σ_{dep} and downwards by the CO condensation temperature. Molecules of CO are present (with a constant abundance $X_u(\text{CO}) = 10^{-4}$) when the H_2 column density from the current (r, z) point to the disk surface (i.e., towards (r, ∞)) exceeds a given threshold Σ_{dep} , reflecting the possible impact of photo-desorption of molecules, or when the temperature $T(r, z)$ is above 17 K. Such a model takes into account the possible presence of CO in the inner disk mid-plane inside the CO snowline radius, and also at large radii because as soon as the surface density becomes low enough, CO emission can again be located on the mid-plane. In this model, the CO surface density radial profile $\Sigma(r) \times X_u(\text{CO})$ (where $\Sigma(r)$ is the H_2 surface density profile) is constrained because there needs to be sufficient opacity for the CO $J = 2-1$ at high altitudes above the disk mid-plane in order to reproduce the observed brightness. The derived H_2 densities are then strictly inversely proportional to the assumed $X_u(\text{CO})$.

Table 2 gives the parameters of the best model we found with this approach. Unfortunately the current angular resolution of the data limits the analysis. Because of this limited angular resolution, parameters T_{atm}^0 , δ , z_q are strongly coupled; z_q also depends implicitly on T_{mid} because it is the number of hydrostatic scale heights at which the atmospheric temperature is reached. In practice, Table 2 only confirms a low mid-plane temperature (10 K at 100 au), and temperatures at least a factor of 2 larger than this in the CO rich region, consistent with the (spatially averaged) values derived in Sect. 3.3. Only higher spatial resolution data would allow us to break the degeneracy and accurately determine the vertical temperature gradient (see Sect. 5.4).

Furthermore, even this model only qualitatively reproduces the brightness distribution of the CO emission around the mid-plane. In particular, the shape of the depletion zone is difficult to evaluate from the current data. We also fail to reproduce the rise of the CO brightness after 250 au, most likely because our model does not include an increase in the temperature in the outer part.

Most chemical models (e.g., Reboussin et al. 2015) predict that there is some CO at low abundance ($X_p(\text{CO}) \sim 10^{-8}-10^{-6}$) in the mid-plane, depending on the grain sizes and the local dust-to-gas ratio, contrary to our simple assumption of $X_p(\text{CO}) = 0$. Such low abundances would not impact our determination of the CO surface density, which only relies on the need to have sufficient optical thickness in the upper layers. However, CO could start being sufficiently optically thick around the mid-plane, diminishing the contrast between the mid-plane and the molecular layer. We estimated through modeling that this happens for

Table 2. Model derived from the CO observations.

Parameter	Value	Unit	Parameters at 100 au
T_{atm}^0	50	K	Atmosphere temperature
q_{atm}	0.4		
z_q	3		
δ	2		
T_{mid}^0	10	K	Mid-plane temperature
q_{mid}	0.4		
Σ_0	10^{23}	cm^{-2}	H_2 surface density
p	0.5		Surface density parameter
R_C	50	au	Radius for exponential decay
H_0	11.3	au	Scale height
h	-1.3		Exponent of scale height
R_{out}	330	au	Outer radius
i	87	$^\circ$	Inclination
Σ_{dep}	10^{22}	cm^{-2}	Surface density for depletion
T_{dep}	17	K	Depletion temperature
$X_{\text{u}}(\text{CO})$	10^{-4}		CO abundance in upper layers
$X_{\text{p}}(\text{CO})$	0		CO abundance in mid-plane
M_{disk}	0.7×10^{-3}	M_\odot	Disk mass

Notes. $\Sigma(r)$ corresponds to Eq. (5) in [Guilloteau et al. \(2011\)](#), $H(r) = H_0(r/100 \text{ au})^{-h}$, and $T(r)$ is defined in Eqs. (1)–(3), this paper. The disk is in Keplerian rotation around a $0.57 M_\odot$. Only the product of $\Sigma_0 \times X_{\text{u}}(\text{CO})$ is constrained by the observations: changing $X_{\text{u}}(\text{CO})$ will change Σ_0 and M_{disk} by the inverse amount.

$X_{\text{p}}(\text{CO}) \geq 3 \times 10^{-8}$. In such cases, the brightness distribution becomes similar to that of the undepleted case. Observations of a less abundant isotopolog would be a better probe of the mid-plane depletion.

We thus conclude that the current data are insufficient to distinguish between molecular depletion and a very cold mid-plane, but indicate a rise in mid-plane temperature beyond 200 au.

In Fig. 7, we overlay the brightness temperature derived from the observations to the structure of the model given in Table 2. The brightness temperature from the model is compared to the observations and is also shown in Fig. 8 at three different angular resolutions of $0.5''$, $0.3''$, and $0.1''$.

5. Discussion

5.1. Overall disk structure

The analysis of the CO and CS brightness temperature patterns shows that there is no significant departure from a simple disk geometry at the linear resolution of 60 au, with the exception of the north-south brightness difference. This may be due to an intrinsic asymmetry; however, the same effect can also be produced if the disk is slightly inclined by a few degrees from edge-on. Owing to the flaring and radial temperature gradient, the optically thick emission of the far side always originates from slightly warmer gas ([Guilloteau & Dutrey 1998](#)). Indeed, we find that an inclination angle of 87° is enough to account for the north-south dissymmetry, with the southern part of the disk being closer to us. This inclination (and orientation) is in very good agreement with that of $86 \pm 1^\circ$ derived by [Grosso et al. \(2003\)](#) from near-infrared (NIR) observations. The brightness distributions of the NIR images also show that the southern part of the disk is closer to us. Finally, there is no apparent sign of warp beyond a radius of about 50 au.

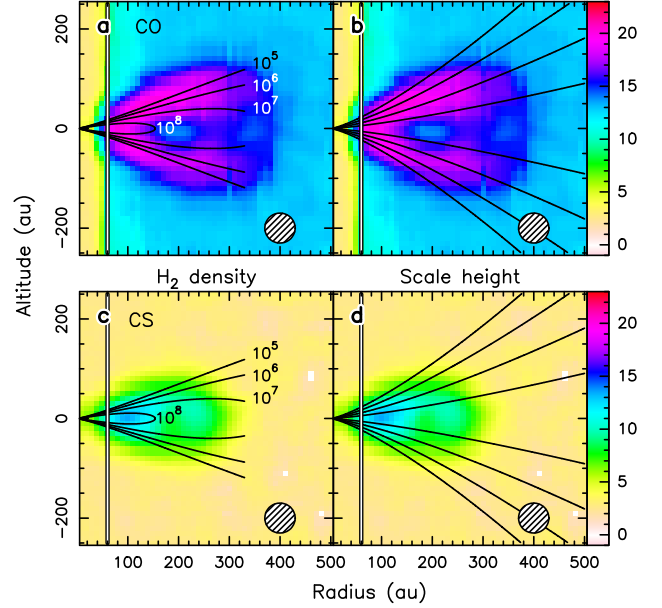


Fig. 7. Superimposition of the CO and CS median TRD to a standard disk model. *a)* CO TRD (color) and the H_2 volume density superimposed in labeled contours from 10^5 up to 10^8 cm^{-3} ; *b)* CO TRD with the scale height superimposed in black contours from 1 to 4 scale heights; *panels c and d* as *panels a and b*, but for CS. The model corresponds to the parameters given in Table 2.

Figure 7 shows that the CO emission is above one scale height, while the CS emission appears slightly below and less extended vertically. This is not surprising because CS $J = 5-4$ is excited only at the high densities near the mid-plane, while CO $J = 2-1$ is easy to thermalize at densities as low as a few 10^3 cm^{-3} (panels a–c of Fig. 7 trace the density distribution). As a consequence, the convolution by the ~ 56 au beam leads to different positions of the peak of the emission layer. The CO layer is vertically resolved and extended, while the CS emission is vertically unresolved and peaks just below one scale height. These vertical locations for the CO and CS layers are consistent with predictions by chemical models (see [Dutrey et al. 2011](#), Fig. 8 where CS peaks between 1 and 2.5 scale heights). A CO layer above the mid-plane has already been observed in the disk of HD 163296 ([de Gregorio-Monsalvo et al. 2013](#); [Rosenfeld et al. 2013](#)).

We also estimate for the first time the amplitude of the vertical temperature gradient between the cold mid-plane, the molecular layer, and the CO atmosphere at radii between 50 and 300 au. The gas vertical temperature gradient derived at 100 au is in agreement with that predicted by thermo-chemical models (e.g., [Cleeves et al. 2016](#)) with a mid-plane at about 8–10 K and a temperature of 25 K reached at two scale heights. The main limitation here is the linear resolution of 60 au. Nevertheless, the observed pattern of the brightness distribution suggests the existence of warmer gas inside a radius of about 50–80 au. Any inner hole of radius < 15 au cannot be seen in these data, due to our sensitivity limit.

5.2. Radial profile of CO near the mid-plane

We discuss here two possible origins for the emission drop in the CO radial profile.

Rise of the CO brightness a large radius: In the upper layers the CO brightness decreases smoothly with radius, while in the

mid-plane we observe a rise in CO brightness beyond a radius of about 200 au. The transition radius coincides with the mm-emitting dust disk outer boundary, ~ 187 au in the simple model from [Guilloteau et al. \(2016\)](#), while in scattered light the disk is nearly as extended as the CO emission ([Grosso et al. 2003](#)). This suggests that a change in grain size distribution may also play a role here. With the dust composed of mostly micron-sized grains better coupled with the gas (see [Pontoppidan et al. 2007](#)), more stellar light may be intercepted and may result in a more efficient heating of the gas, as suggested by recent chemical models ([Cleeves 2016](#)). Moreover, at the expected densities in the disk mid-plane, the dust and gas temperatures should be strongly coupled; a dust temperature rise is also naturally expected when the disk becomes optically thin to the incident radiation and for the re-emission, as shown by, e.g., [D'Alessio et al. \(1999\)](#).

Also, as the ρ Oph region is bathed in a higher-than-average UV field due the presence of several B stars, this effect may be reinforced by additional heating due to a stronger ambient UV field. However, the Flying Saucer is located on the eastern side of the dark cloud, whose dense clouds absorb the UV from the B stars, located mainly on the western side. Figures 1a and 4a in [Lim et al. \(2015\)](#) show that there is a clear dip in the far-UV emission due to the dark cloud silhouette. Therefore, at the location of the Flying Saucer ($l = 353.3$, $b = 16.5$) the ambient far-UV field cannot be very large.

Apparent gap at radius 185 au: The presence of an apparent gap at ~ 185 au in both CO and CS is puzzling. Its existence in CO indicates that a change in temperature and/or beam dilution is the primary cause for this deficit, as CO is easily thermalized and optically thick. This suggests that the disk mid-plane warms up beyond this radius, before the emission fades again near the disk edge (on the order of ~ 330 au) where CO becomes optically thin and CS unexcited.

An alternative explanation is that it is the result of a real gap in the molecular distribution, smoothed out by our limited angular resolution. The optically thick CO line traces material at low and at high altitude (up to 3–4 scale heights above the mid-plane), while CS $J = 5-4$, a high density tracer, is more optically thin and is only observed in high density regions (at typically one scale height). Contrary to a face-on or inclined disk, the gap can be seen in ^{12}CO because the disk is edge-on.

The brightness minimum at 185 au is only seen at low altitudes, typically between the mid-plane and an altitude of 40 au in CO, and slightly higher in CS, so the putative gap cannot extend upwards in the disk. This morphology remains consistent with expectations for gaps created by planets, provided the Hills radius is smaller than the disk scale height.

5.3. Deriving the gas density from CS excitation conditions

In CS $J = 5-4$, we observe a similar north-south asymmetry to that in CO $J = 2-1$. This indicates that the emission has a substantial optical thickness along the line of sight.

The brightness ratio of CS over CO is within the range 0.5–0.7 until a radius of about 250 au and drops quickly beyond. As indicated by the iso-density contours shown in Fig. 7, this is consistent with the decreasing H_2 density with radius because the CS $J = 5-4$ transition is thermalized at a few 10^6 cm^{-3} ([Denis-Alpizar et al., in prep.](#)).

On the contrary, the observed ratio of 0.5–0.7 in the inner disk mid-plane cannot be explained by excitation conditions. A simple escape probability calculation using the CO freeze out

temperature $T_k = 17 \text{ K}$ (which is in agreement with the CS temperature derived from the simple analysis), a surface density of $4 \times 10^{13} \text{ cm}^{-2}$, and a local line width of 0.3 km s^{-1} (obtained from a simple analysis with DiskFit using a power law surface density distribution) yields $T_{\text{ex}} = 12 \text{ K}$ for a density of 10^6 cm^{-3} . This density is much lower than expected in the disk given the dust emission observed at mm wavelengths, and lower than the values derived from our CO modeling.

The ratio is better explained as resulting from different beam dilutions in CO and CS. At 200 au, the CO emission is spatially resolved, while the region emitting in CS $J = 5-4$ must fill only 50% of the synthesized beam, i.e., must have a thickness of only ~ 30 au. The emission peak being located ~ 45 au above the plane at this radius, the CS emitting layer must be confined between about 30 and 60 au there. Furthermore, the density at $r = 200$ au and $z = 60$ au is about 10^6 cm^{-3} in our fiducial disk model, so that the upper layers are no longer dense enough to excite the $J = 5-4$ line. Hence the observed CS/CO brightness ratio is roughly consistent with a molecular layer extending above one scale height, with subthermal excitation of the CS $J = 5-4$ transition truncating the CS brightness distribution upwards.

In this interpretation, the CS layer is expected to be thinner for higher J transitions. An angular resolution around $0.2''$ would be needed to resolve the CS layer.

At smaller radii, the CO and CS layer both become unresolved vertically, but the ratio of their respective thickness is not expected to change significantly, leading to a nearly constant brightness ratio.

5.4. Limits: angular resolution, local line width, and inclinations

Figure 8 shows the TRD of the model obtained with DiskFit assuming CO depletion around the mid-plane at three different angular resolutions, $0.5''$, $0.3''$, and $0.1''$. The impact of the resolution on this apparent brightness distribution is striking. For comparison, the intrinsic temperature $T(r, z)$ distribution is shown in panel (g) for all points where the H_2 density exceeds 10^4 cm^{-3} . Panels (f) and (g) show the impact of the small Keplerian shear compared to the local line width at the disk edge (which spreads the TRD beyond the outer disk radius, see Sect. 4.1), and of the small deviation from a pure edge-on disk (which results in a top/bottom asymmetry). For this specific disk structure, the peak brightness is lowered by a factor of 2 when degrading the angular resolution from $0.1''$ to $0.5''$. The inner CO disk, the radius of the CO snowline, and the whole gas distribution can be resolved at $0.1''$, but not at $0.5''$. The stratification of the molecular layer can only be studied at $0.1''$ resolution, down to about 30 au where the scale height becomes too small compared to the linear resolution for a direct measurement. We also observe a displacement of the peak brightness towards larger radii at $0.5''$ resolution compared to its (true) location at $0.1''$ resolution, which occurs because the vertical extent of the CO emission at large radii is larger, due to the flaring. Finally, at $0.5''$ we find that it is not possible to determine the shape of the (partly) depleted zone around the mid-plane beyond the CO snowline radius. Even a resolution of $0.3''$ would allow the measurement of the depletion factor (and estimate of the CO/dust ratio) around the mid-plane while an angular resolution of $0.1''$ would in addition allow us to determine the shape of this area.

Besides angular resolution and local line width, inclination is another limitation of the method. To the first order, the disk should be edge-on to within $h(r)/r$ for the TRD to be directly useable, i.e., in the range $80-90^\circ$ given the typical $h(r)/r$ of disks

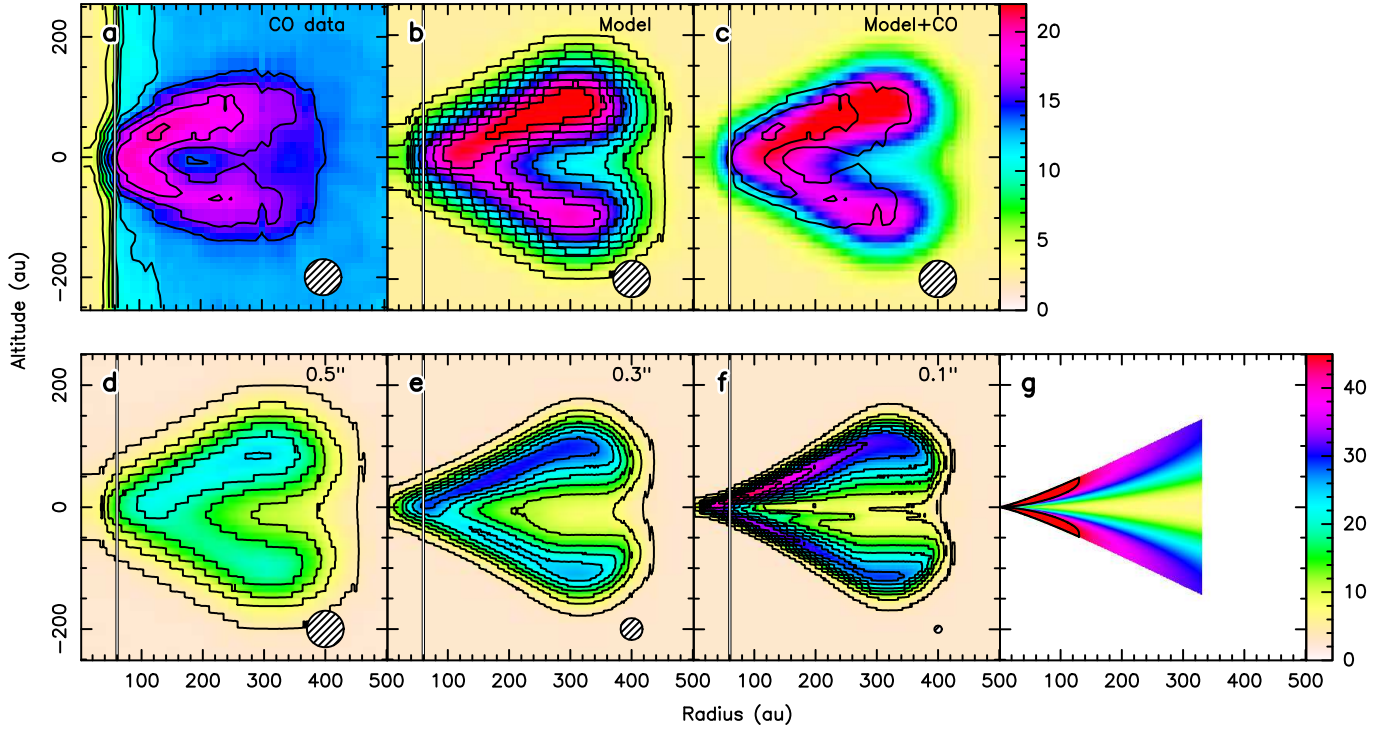


Fig. 8. TRD for CO $J = 2-1$ (in Kelvin). *a*) Observed CO TRD; *b*) best model; *c*) CO TRD in false color with best model in black contours; *d*) model at $0.5''$ or 60 au resolution; *e*) model at $0.3''$ or 36 au resolution and *f*) at $0.1''$ (12 au) resolution, presented with the same color scale (contours in 4 K steps); *g*) initial temperature distribution (black contour at 45 K).

at 100–300 au. However, even for somewhat lower inclination, the TRD can give insight into the location of the molecular layer. We illustrate this in Appendix B.

These simulations clearly demonstrate how well ALMA can characterize the structure of an edge-on protoplanetary disk, provided its distance is reasonable.

6. Summary

We report an analysis of the CO $J = 2-1$ and CS $J = 5-4$ ALMA maps of the Flying Saucer, a nearly edge-on protoplanetary disk orbiting a T Tauri star located in the ρ Oph molecular cloud. At the angular resolution of $0.5''$ (60 au at 120 pc) and in spite of some confusion in CO due to the background molecular clouds, we find the following:

- the disk is in Keplerian orbit around a $0.57 M_{\odot}$ star and nearly edge-on (inclined by 87°). It does not exhibit a significant departure from symmetry in CO or in CS;
- direct evidence of a vertical temperature gradient is demonstrated by the CO emission pattern; however, quantitative estimates are limited by the spatial resolution;
- distinguishing between CO depletion and very low temperatures is not possible because of the limited angular resolution. Models with CO depletion in the mid-plane only agree marginally better, and the mid-plane temperature cannot be significantly larger than 10 K at 100 au;
- the CO emission is observed between 1 and 3 scale heights, while the CS emission is located around one scale height. Subthermal excitation of CS may explain this apparent difference;
- CO is also observed beyond a radius of 230–260 au, in agreement with models predicting a secondary increase of temperature due to higher UV flux penetration in the outer disk.

However, the limited angular resolution does not rule out an alternate explanation with a molecular gap near 185 au.

Finally, our results demonstrate that observing an edge-on disk is a powerful method of directly sampling the vertical structure of protoplanetary disks provided the angular resolution is high enough. At least one data set with angular resolution around $0.1-0.2''$ is needed for a source located at 120–150 pc.

Acknowledgements. We thank the referee for constructive comments. This work was supported by “Programme National de Physique Stellaire” (PNPS from INSU/CNRS). This research made use of the SIMBAD database, operated at the CDS, Strasbourg, France. This paper makes use of the following ALMA data: ADS/JAO.ALMA#2013.1.00387.S. ALMA is a partnership of ESO (representing its member states), NSF (USA), and NINS (Japan), together with NRC (Canada), NSC and ASIAA (Taiwan), and KASI (Republic of Korea) in cooperation with the Republic of Chile. The Joint ALMA Observatory is operated by ESO, AUI/NRAO, and NAOJ. This paper is based on observations carried out with the IRAM 30 m telescope. IRAM is supported by INSU/CNRS (France), MPG (Germany), and IGN (Spain). V.W.’s research is funded by the European Research Council (Starting Grant 3DICE, grant agreement 336474).

References

- ALMA Partnership, Brogan, C. L., Pérez, L. M., et al. 2015, *ApJ*, **808**, L3
 Andrews, S. M., Wilner, D. J., Hughes, A. M., et al. 2012, *ApJ*, **744**, 162
 Andrews, S. M., Wilner, D. J., Zhu, Z., et al. 2016, *ApJ*, **820**, L40
 Beckwith, S. V. W., & Sargent, A. I. 1993, *ApJ*, **402**, 280
 Bergin, E. A., Cleeves, L. I., Gorti, U., et al. 2013, *Nature*, **493**, 644
 Chapillon, E., Guilloteau, S., Dutrey, A., Piétu, V., & Guélin, M. 2012, *A&A*, **537**, A60
 Cleeves, L. I. 2016, *ApJ*, **816**, L21
 Cleeves, L. I., Öberg, K. I., Wilner, D. J., et al. 2016, *ApJ*, **832**, 110
 D’Alessio, P., Calvet, N., Hartmann, L., Lizano, S., & Cantó, J. 1999, *ApJ*, **527**, 893
 Dartois, E., Dutrey, A., & Guilloteau, S. 2003, *A&A*, **399**, 773
 de Gregorio-Monsalvo, I., Ménard, F., Dent, W., et al. 2013, *A&A*, **557**, A133
 Dutrey, A., Wakelam, V., Boehler, Y., et al. 2011, *A&A*, **535**, A104

- Gorti, U., Hollenbach, D., Najita, J., & Pascucci, I. 2011, [ApJ](#), **735**, 90
- Grosso, N., Alves, J., Wood, K., et al. 2003, [ApJ](#), **586**, 296
- Guilloteau, S., & Dutrey, A. 1998, [A&A](#), **339**, 467
- Guilloteau, S., Dutrey, A., Piétu, V., & Boehler, Y. 2011, [A&A](#), **529**, A105
- Guilloteau, S., Piétu, V., Chapillon, E., et al. 2016, [A&A](#), **586**, L1
- Lim, T.-H., Jo, Y.-S., Seon, K.-I., & Min, K.-W. 2015, [MNRAS](#), **449**, 605
- Loinard, L., Torres, R. M., Mioduszewski, A. J., & Rodríguez, L. F. 2008, [ApJ](#), **675**, L29
- Piétu, V., Dutrey, A., & Guilloteau, S. 2007, [A&A](#), **467**, 163
- Pontoppidan, K. M., Stapelfeldt, K. R., Blake, G. A., van Dishoeck, E. F., & Dullemond, C. P. 2007, [ApJ](#), **658**, L111
- Qi, C., Ho, P. T. P., Wilner, D. J., et al. 2004, [ApJ](#), **616**, L11
- Qi, C., Öberg, K. I., Wilner, D. J., et al. 2013, [Science](#), **341**, 630
- Reboussin, L., Guilloteau, S., Simon, M., et al. 2015, [A&A](#), **578**, A31
- Rosenfeld, K. A., Qi, C., Andrews, S. M., et al. 2012, [ApJ](#), **757**, 129
- Rosenfeld, K. A., Andrews, S. M., Hughes, A. M., Wilner, D. J., & Qi, C. 2013, [ApJ](#), **774**, 16
- Schwarz, K. R., Bergin, E. A., Cleeves, L. I., et al. 2016, [ApJ](#), **823**, 91
- Teague, R., Guilloteau, S., Semenov, D., et al. 2016, [A&A](#), **592**, A49
- Teague, R., Semenov, D., Gorti, U., et al. 2017, [ApJ](#), **835**, 228
- Thi, W.-F., Mathews, G., Ménard, F., et al. 2010, [A&A](#), **518**, L125
- van Boekel, R., Henning, T., Menu, J., et al. 2017, [ApJ](#), **837**, 132
- Weidenschilling, S. J. 1977, [MNRAS](#), **180**, 57

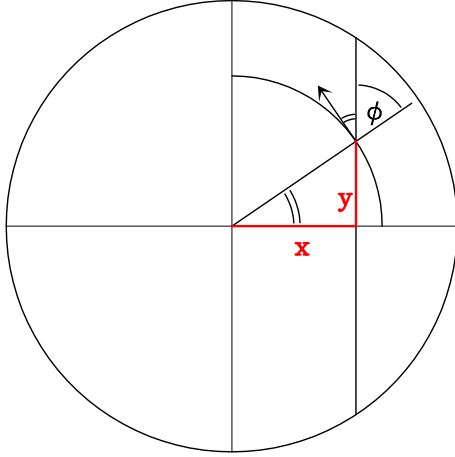


Fig. A.1. Definition of notations.

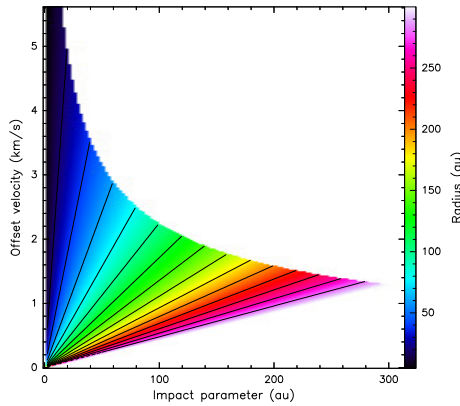


Fig. A.2. Radius as a function of position and velocity for an edge-on Keplerian disk

Appendix A: position-velocity diagram for an edge-on Keplerian disk

Let x be the impact parameter in the disk, y the coordinate along the line of sight, and r the radial distance

$$r(y) = \sqrt{x^2 + y^2}, \quad (\text{A.1})$$

where $y < y_m$, with y_m given by

$$y_m = \sqrt{R_d^2 - x^2} \quad (\text{A.2})$$

The angle ϕ is defined such that $x = r \sin \phi$ (see Fig. A.1). The projected velocity along the line of sight is

$$V_y = \sqrt{GM/r} \sin \phi = \sqrt{GM/r} \frac{x}{r} = \sqrt{GM} \frac{x}{r^{3/2}} \quad (\text{A.3})$$

Thus we simply recover r

$$r = \left[GM \left(\frac{x}{V_y} \right)^2 \right]^{1/3} = R_d \left(\frac{X}{V} \right)^{2/3}, \quad (\text{A.4})$$

where $X = x/R_d$, $V = V_y/V_d$, and $V_d = \sqrt{GM/R_d}$ is the rotation velocity at the outer disk radius. Since $x \leq r \leq R_d$, the above equation has a solution provided $X < V < 1/\sqrt{X}$ (i.e., $V_y > V_d x/R_d$, and $V_y < \sqrt{GM/x}$). So, for any given velocity V_y and impact parameter x , we can solve for r , and then recover $y = \pm \sqrt{r^2 - x^2}$ along the line of sight.

As a consequence, in the PV diagram (showing functions of (x, V)) of a Keplerian disk, any line starting from $(x = 0, V = V_{\text{sys}})$ represents locii of constant radius. This is illustrated in Fig. A.2. We use this property to directly recover the temperature as a function of radius (by taking the mean or the median for any given r) and altitude (by making cuts in the PV diagrams for different altitudes).

For optically thick lines, this procedure yields the (beam averaged) excitation temperature, and thus the kinetic temperature if the line is thermalized.

For optically thin lines, the opacity is a function of (r, x) because of the Keplerian shear which breaks the rotational symmetry. The above procedure thus yields a more complex function of the temperature and density, those values, however, cannot exceed the excitation temperature at any radius r .

Appendix B: Inclination effects

Figure B.1 shows the expected TRDs of our fiducial disk model (Table 2) for different disk inclinations. In this model, CO emits mostly 1 or 2 scale heights above the disk mid-plane, thus when the inclination differs from edge-on by more than $h(r)/r$, the two opposite layers can project on the same side compared to the mid-plane projection. The farthest part of the disk projects to positive altitudes in Fig. B.1. It appears warmer than the projection of the nearest part because for the same impact parameter in altitude, the line of sight intercepts first warm gas due to the disk flaring; for the nearest part, the warm gas is hidden behind the forefront colder regions (see Dartois et al. 2003). The depletion in the mid-plane makes a clear distinction between the two emitting cones in the disk, resulting in a bright double layer at positive altitudes for $i = 70-75^\circ$. At lower inclinations, the projected velocity gradient becomes insufficient to clearly separate these two layers on the TRD. For $i = 80-85^\circ$, the two layers no longer project on the same side: a small lukewarm “finger” of emission appears at an altitude around -20 au.

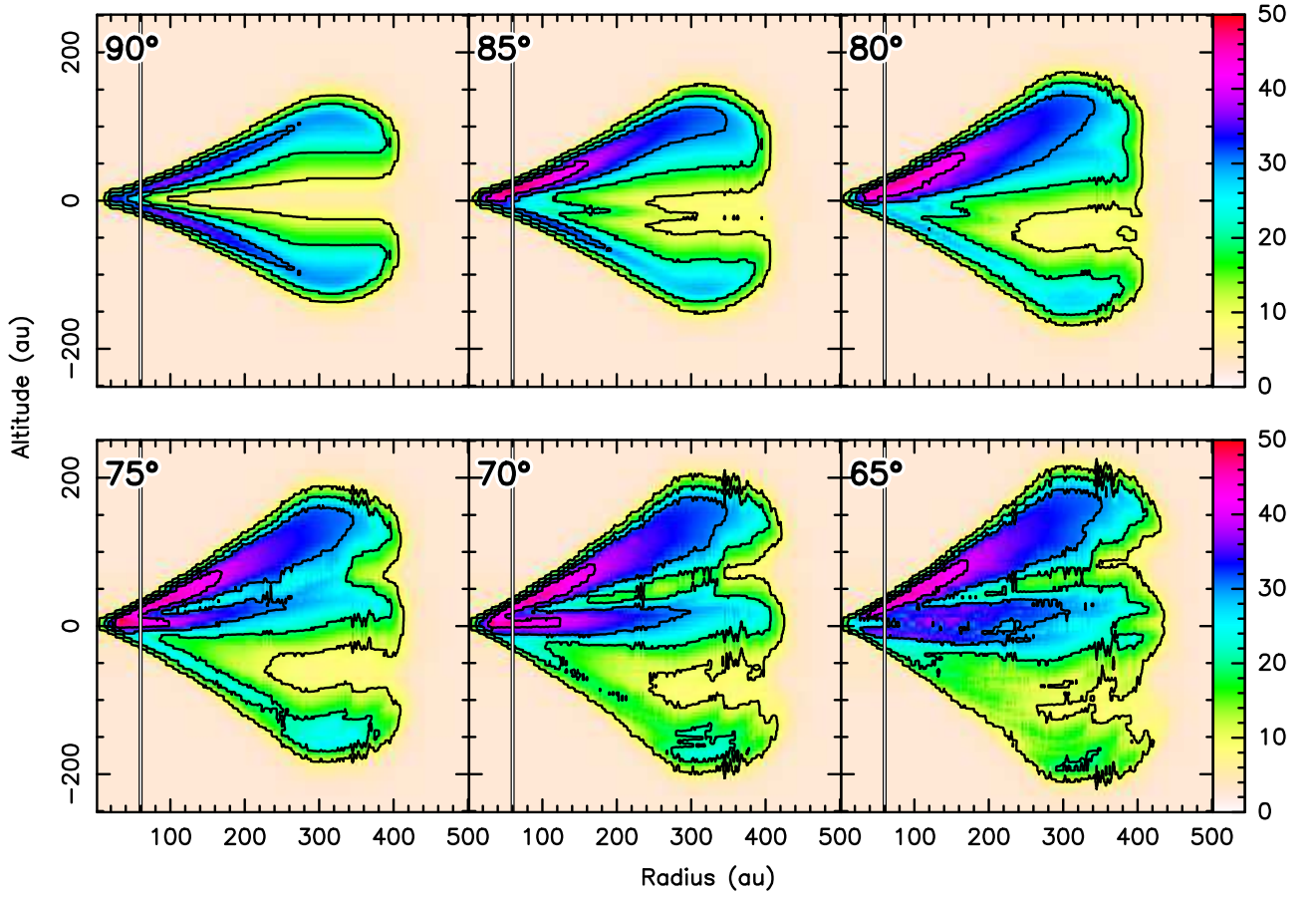


Fig. B.1. TRD for CO $J = 2-1$ (in kelvin) of our best disk model for different inclinations. Contours are in 10 K steps.